

**GRADUATE AEROSPACE LABORATORIES**  
**CALIFORNIA INSTITUTE OF TECHNOLOGY**  
Pasadena, California 91125

**DISPERSION, MIXING, AND COMBUSTION IN UNIFORM- AND VARIABLE-  
DENSITY AIR-BREATHING HIGH-SPEED PROPULSION FLOWS**

Paul E. Dimotakis (PI), Caltech

Air Force Office of Scientific Research  
AFOSR Grant FA9550-10-1-0262

Final Performance Report for the period  
15 June 2010 to 14 June 2013

28 August 2013

## Report Documentation Page

*Form Approved*  
*OMB No. 0704-0188*

Public reporting burden for the collection of information is estimated to average 1 hour per response, including the time for reviewing instructions, searching existing data sources, gathering and maintaining the data needed, and completing and reviewing the collection of information. Send comments regarding this burden estimate or any other aspect of this collection of information, including suggestions for reducing this burden, to Washington Headquarters Services, Directorate for Information Operations and Reports, 1215 Jefferson Davis Highway, Suite 1204, Arlington VA 22202-4302. Respondents should be aware that notwithstanding any other provision of law, no person shall be subject to a penalty for failing to comply with a collection of information if it does not display a currently valid OMB control number.

1. REPORT DATE <b>28 AUG 2013</b>	2. REPORT TYPE	3. DATES COVERED <b>15-06-2010 to 14-06-2013</b>			
4. TITLE AND SUBTITLE <b>Dispersion, mixing, and combustion in uniform- and variable-density air-breathing high-speed propulsion flows</b>		5a. CONTRACT NUMBER			
		5b. GRANT NUMBER			
		5c. PROGRAM ELEMENT NUMBER			
6. AUTHOR(S)		5d. PROJECT NUMBER			
		5e. TASK NUMBER			
		5f. WORK UNIT NUMBER			
7. PERFORMING ORGANIZATION NAME(S) AND ADDRESS(ES) <b>Graduate Aerospace Laboratories, California Institute of Technology, 1200 E. California Blvd., Pasadena, CA, 91125</b>		8. PERFORMING ORGANIZATION REPORT NUMBER			
9. SPONSORING/MONITORING AGENCY NAME(S) AND ADDRESS(ES)		10. SPONSOR/MONITOR'S ACRONYM(S)			
		11. SPONSOR/MONITOR'S REPORT NUMBER(S)			
12. DISTRIBUTION/AVAILABILITY STATEMENT <b>Approved for public release; distribution unlimited</b>					
13. SUPPLEMENTARY NOTES					
14. ABSTRACT					
15. SUBJECT TERMS					
16. SECURITY CLASSIFICATION OF:			17. LIMITATION OF ABSTRACT	18. NUMBER OF PAGES	19a. NAME OF RESPONSIBLE PERSON
a. REPORT <b>unclassified</b>	b. ABSTRACT <b>unclassified</b>	c. THIS PAGE <b>unclassified</b>	<b>Same as Report (SAR)</b>	<b>28</b>	

## Summary/overview

This is the final technical report on significant work accomplished as part of a fundamental-research effort undertaken at Caltech, in collaboration with researchers at other universities. The work combined experiments, numerical simulations, modeling, and a diagnostics-/instrumentation-development effort. Work performed as part of this effort spans a pre-award period from 1 December 2009 through 14 June 2010, and the period of performance from 15 June 2010 to 14 June 2013. Some of the work and progress described below was cosponsored by the AFOSR MURI under Grant No. FA9550-07-1-0091. Parts have also led to efforts presently in progress, funded under AFOSR Grant No. FA9550-12-1-0461. These focus on related topics relevant to energy-release effects in supersonic air-breathing propulsion flows.

## Abstract

This is a summary of significant accomplishments in investigations on the dispersion, mixing, and combustion in uniform- and variable-density air-breathing high-speed propulsion flows related to scramjet propulsion. In experimental work, progress made in the development of test-section modifications allowed inclined-jet injection in supersonic flow to be studied with and without chemical reactions and heat release. Work on hydrocarbon flames was completed and published, and preliminary investigations on high-pressure effects were conducted. Large-eddy simulations (LES) were performed on chemically reacting flows in complex geometries, achieving both grid convergence and agreement with experiment. The same computational framework was successfully applied to simulations of inclined-jet injection into a supersonic Mach 3.6 stream. A model for an ethylene-fueled scramjet was developed to facilitate parametric studies of ignition delays in flight-relevant environments. Accomplishments in diagnostic developments enabled many of the experiments and included high framing-rate schlieren digital-imaging technologies, two-dimensional temperature-field measurement technologies, advances in data processing and visualization, and advances in multi-component computer control of experiments.

## 1. Introduction

The viability of scramjet propulsion at the low end of its anticipated flight Mach number range is challenged by a variety of issues including cycle-efficiency considerations (Heiser & Pratt 1994), choking and unstart issues attributable to mass injection, skin (wall) friction and boundary-layer displacement effects, compounded by boundary-layer displacement increases as a result of shock-wave boundary-layer interactions in both the isolator and combustor sections, thermal choking, and limitations arising from finite chemical kinetics and combustion efficiency. Ignition delays and required combustion-completion times present particular challenges for scramjet powered flight in the low Mach number regime in that chemical reactions must be preceded by mixing on a molecular scale that has been documented to be less efficient at hypersonic speeds. The experimental sections of this report focus on issues of choking and unstart attributable to mass injection, skin friction and boundary-layer displacement effects, and thermal choking. Part of the objective of this research effort is to investigate dispersion, mixing, and increase choking margins, using complex flow geometry, including recirculation zones, and fuel injection exploiting shear-layer, jet-in-crossflow, as well as both in combination.

A section of this report focuses on chemical-kinetic limitations, specifically ignition delays, and describes a parametric study relating ignition delay distances to flight and inlet conditions, and injected-fuel conditions for a generic ethylene-fueled scramjet. The objective of the latter effort is to develop a methodology to generate scaling laws for scramjet design, and to motivate research efforts in fuel injection, mixing and combustion for hypersonic flight.

## 2. Technical discussion

Research undertaken combined work performed on experimental work on high-speed flows, and scalar dispersion in turbulent flow; numerical simulations and modeling of jet injection into supersonic flow, and dispersion, mixing, and chemical reactions of flow past a rearward-facing ramp at high Reynolds number; modeling of ethylene-fueled scramjet ignition delays; and diagnostics developments in optics, precision thermometry arrays for use in supersonic flows, digital control of a short running-time flow facility, and precision digital control of fluid injection for studies on scalar dispersion.

A description of this work is documented below.

### 2.1 Experimental work

Experimental work focused on the primary goals of this research effort related to supersonic and high-speed flows in general. Part of the experimental effort, however, focused on studies on scalar plumes and dispersion whose behavior is relevant to fuel-injection in propulsion devices. The latter investigations were conducted in water that allows precise and novel field-diagnostic techniques to be employed, so those results play an abstract value in the main focus of this work.

However, they have also proven invaluable in understanding small-scale dispersion and behavior as must be captured by subgrid-scale (SGS) models in large-eddy simulation (LES) models of complex flows.

### 2.1.1 Experiments on high-speed flows

Considerable progress was made and preparatory work was completed in support of reacting runs in the supersonic shear-layer and jet-injection facility. See Figure 1 for a test-section facility schematic and Figure 2 for a digital image.

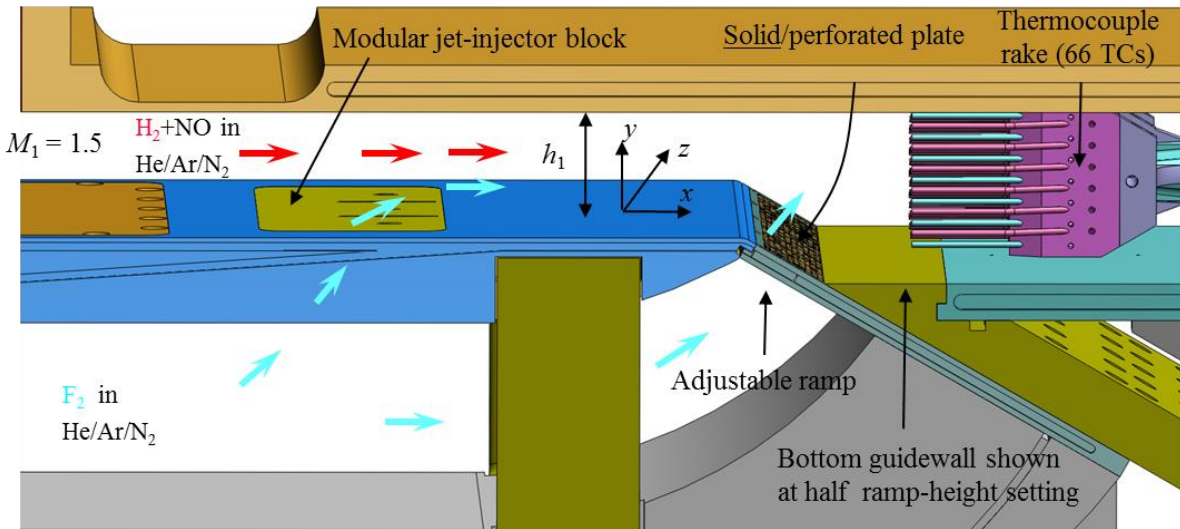


Figure 1. Schematic of supersonic shear-layer facility, showing the angled ramp, jet-injector block, and 2-D thermocouple rake.

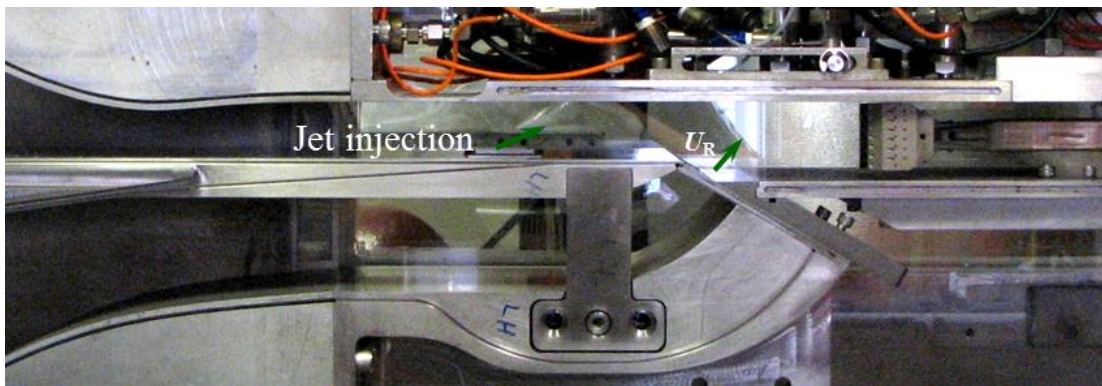


Figure 2. Digital image of the test-section layout schematically indicated in Figure 1. The test section is sandwiched between sidewalls comprised of thick optical-quality BK7 glass walls with interior sacrificial 0.1 inch-thick polished pyrex walls.

The previously developed rake failed under supersonic aerodynamic loads and one of its three columns was removed to decrease blockage for an interim set of runs. A new thermocouple rake

was designed, fabricated, and calibrated to high accuracy that has survived the harsh dynamic and chemical environment and used for all recent runs. In particular, the thermocouple set was recalibrated to obtain a temperature precision of  $|\delta T| \leq 0.15\text{K}$ , as discussed below.

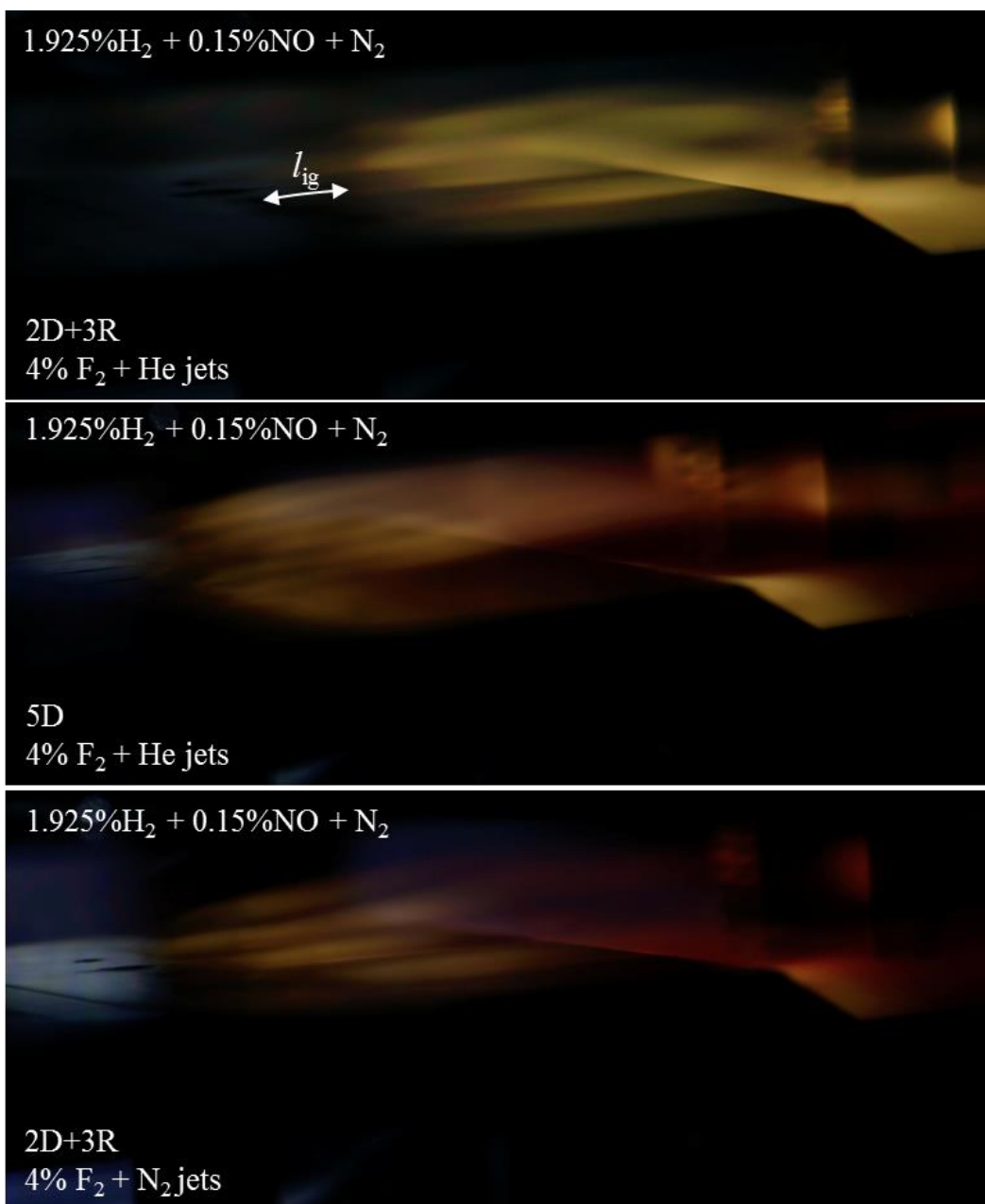


Figure 3. Reacting chemiluminescence images with supersonic ( $M_1 = 1.5$ ) upper streams. Composition and diluents, as indicated. Top: Jet injection through two diamond and three round jets (He jet-fluid diluent). Middle: Jet injection through 5 diamond jets (He jet-fluid diluent). Bottom: Jet injection through two diamond jets and three round jets ( $\text{N}_2$  jet-fluid diluent). Data from Mehrotra, Maddalena, Lang, and Dimotakis (unpublished).

Reacting and non-reacting runs were performed based on inclined-jet injection with no ramp injection (solid ramp). These were diagnosed with precision thermometry, simultaneously with high-speed schlieren, chemiluminescence imaging for the reacting runs, and wall-pressure measurements.

Figure 3 reproduces chemiluminescence images from three runs with a supersonic upper stream at  $M_1 = 1.5$ , chemical and diluent compositions as indicated. The upper stream diluent is nitrogen for all experiments. Except for the jet injector configurations, the geometry is common to all three. The locations of the inclined-jet penetrations through the jet-injector block top surface best discernible in the bottom image. The 30 degree rearward-facing ramp wall is solid (no ramp injection). See also Figure 4 and Figure 5, and associated discussion below.

Chemiluminescence is a relatively fast indicator of chemical reactions in progress and indicates the spatial region where the chemical reactions occur. Several features in the images in Figure 3 are noteworthy.

1. Tracing the chemiluminescence to the two kinds of jets, one can distinguish the difference in penetration between the round and diamond jets, with the former remaining closer to the wall and the latter penetrating deeper.
2. The difference in luminosity in the separated-flow region behind the rearward-facing ramp can be attributed to the difference in penetration between the round and diamond jets. In particular, a much reduced luminous region behind the rearward-facing ramp can be seen in the flow corresponding to the middle image which is generated with diamond jets only.
3. The ignition delay attributable to the delay in mixing followed by the short but finite chemical-reaction rate is visible. The spatial extent,  $l_{\text{ign}}$ , starting from the emerging-jet penetration on the upper surface, corresponding to this delay is indicated in the top image and can be seen to characterize all three geometries.

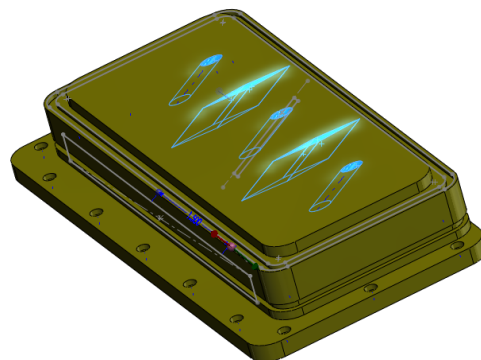


Figure 4. Round and diamond injector orifices, inclined at 30 degrees to the block top surface.

Interpretation of the chemically reacting image data is aided by the simultaneous digital schlieren-image data recorded for these runs (and one more) depicted in Figure 5. Jet injection in all cases is sonic.

The data are single-frame images extracted from high framing rate, 5 – 10 kfps (kilo-frames/s), digital movies. The top, third, and fourth images are from the same runs as for the three in Figure 3. In the run recorded in the second image from the top, the temperature rise (heat release) was double that for the flow recorded in the top frame. The difference in penetration between the round and diamond jets is discernible, with the flow generated by the downstream progression of the round jets hugging the wall and the leading edge of the diamond jets seen penetrating to, approximately, half the supersonic duct height.

The difference in the angular extent of the expansion-wave system is also noteworthy and measures the location (initial angle) of the dividing streamline embedded in the shear layer separating the subsonic recirculation zone from the supersonic flow above it.

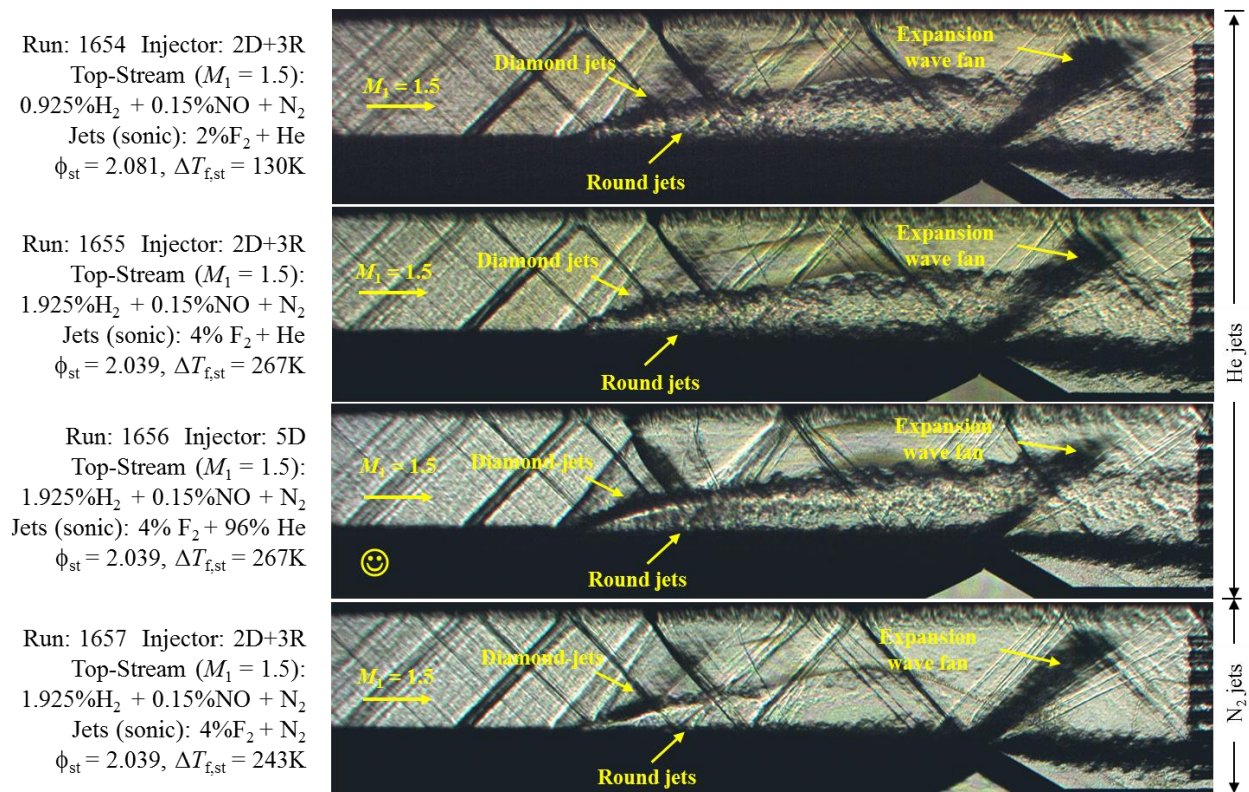


Figure 5. Digital schlieren images for the runs from which the chemiluminescence data are reproduced in Figure 3 (plus one more). Top, third, and fourth images are for the same runs as in Figure 3. In the run recorded in the second image from the top the temperature rise (heat release) doubled that for the flow recorded on top. Experimental parameters as indicated. Data from Mehrotra, Maddalena, Lang, and Dimotakis (unpublished).

A set of non-reacting baseline runs was compiled and analyzed for effects of mass flux, area divergence, and skin friction. This data will be used to isolate heat-release effects on the flow.

Post-processing data-analysis software was written to effectively handle the large volume of time-dependent flow-visualization data, along with temperature and wall-pressure data recorded during each run. Further discussion on significant accomplishments on data visualization and processing is included in Section 1.3.2 on optical diagnostics and data processing below.

The test section and injectors were also characterized for flow parameters including discharge coefficients. Injection mass flux,  $\dot{m}_i$ , was derived from precise measurements of pressure blow-down time sequences. From the geometry of the inclined diamond and circular injectors (Figure 4), their discharge coefficients,  $c_d$ , and their effective discharge area,  $A_{\text{eff}} = c_d A$ , were estimated. The resulting values are given in Table 1 and are of archival value. They can be used to provide accurate estimates of injected mass flow rate through such inclined-jet orifices, requiring only a measurement of the pressure and temperature in the supply plenum.

Table 1. Experimentally estimated discharge coefficients and orifice effective areas,  $A_{\text{eff}} = c_d A$ .

Geometry	$C_d$	Effective area (mm <sup>2</sup> )
Diamond, 30°	0.79	11.4
Round, 30°	0.77	5.6

As also mentioned above, this part of the experimental effort focusing on dispersion and mixing has set the stage for the continuing effort with a redirected goal targeting the effects of heat release and geometry on start/unstart dynamics. It has been the result of the combined effort of Luca Maddalena,<sup>1</sup> Prakhar Mehrotra, Niccolo Cymbalist, Daniel Lang, Bahram Valiferdowski, and Paul Dimotakis.

### 2.1.2 Hydrocarbon flames

During the period of performance and support under this grant, work was completed partly based on recent experimental and theoretical research performed at Caltech on premixed hydrocarbon flames under this grant, along with additional modeling at McGill University. It was published by Bergthorson,<sup>2</sup> Salusbury,<sup>2</sup> and Dimotakis (2011) as “Experiments and modelling of premixed laminar stagnation flame hydrodynamics.”

A new facility to investigate the effects of pressure on laminar premixed CH<sub>4</sub>-air flames in stagnation-flow geometry was completed at Caltech, dubbed the Variable Pressure Flame Facility. Experiments over a range of pressures were conducted and CH-radical location was measured with CH-PLIF, as a function of flame strain rate that was estimated from high resolution particle-tracking velocimetry (PTV) measurements through the flame. The facility design allowed PLIF and PTV data to be recorded simultaneously. Flame instabilities and aero-optical effects were minimized to allow measurements at  $p = 1, 2, 5, 7,$  and  $10$  atm. Despite the high Reynolds numbers corresponding to this flow, careful low-turbulence wind-tunnel

<sup>1</sup> Presently, Assistant Professor at the University of Texas at Arlington.

<sup>2</sup> Presently, Assistant Professor, McGill University, Canada.

technologies were employed resulting in stable-flame operation established throughout this pressure regime (see Figure 6). However, the higher index of refraction associated with higher pressures was responsible for aero-optical effects that may preclude quantitative analysis of optical data for  $p = 10$  atm and above.

This part of the research was conducted by P. Bardet<sup>3</sup> and P. Dimotakis. Work in 2010 reported here concluded research begun under a previous AFOSR grant and was largely supported by Caltech funds.

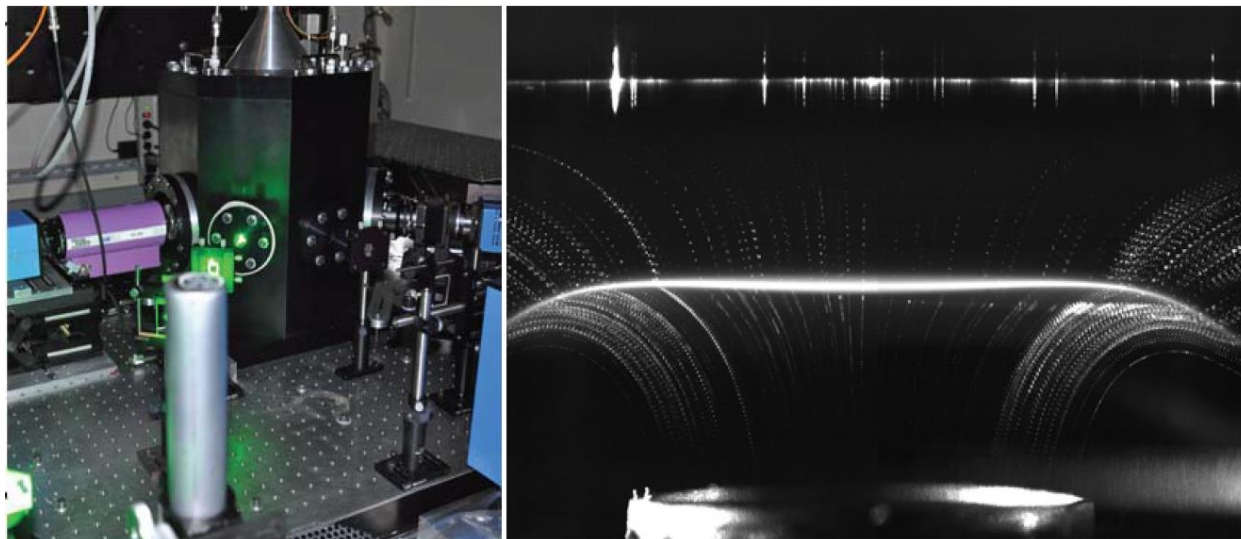


Figure 6. Left: Variable Pressure Flame Facility. Right:  $\text{CH}_4$ -air,  $p = 5$  atm,  $\Phi = 0.85$ , with He as a co-flow and background gas, minimizing aero-optical effects. Particle-tracking velocimetry (PTV) trajectories are reliably quantifiable.

### 2.1.3 Experiments on scalar dispersion

Work on scalar dispersion and mixing focused on the dispersion of a passive scalar in a classical turbulent flow generated by a moving grid (grid-turbulence). The fundamental questions asked, for which there are no definitive answers as yet, is how quickly does a passive scalar (Lagrangian) marker injected into a well-characterized turbulent flow disperse and mix. Does flow Reynolds number play a role? Does the momentum (thrust) with which the injectant is introduced into the turbulent flow play a role? What are the similarity properties of the resulting plume and what is the two- and three-dimensional structure of the resulting scalar field?

The questions are important in understanding fuel injection in turbulent flows in the broad context of air-breathing and high-speed propulsion. Even though the latter take place in air under supersonic-flow conditions, many generic issues are the same.

The scalar-dispersion experiments undertaken required the design and fabrication of a computer-controlled facility and diagnostics, and the ability to record precision measurements of injection

<sup>3</sup> Presently, Assistant Professor, George Washington University.

rate along with scalar concentration as an assembly of two-dimensional slices (transects) in grid-generated turbulence. This is, perhaps, the most-studied turbulent flow. Such slices can later be assembled to form a two-dimensional sequence vs. time, or a three-dimensional sequence vs. time, the latter requiring high-enough frame-sampling rates.

A digitally-controlled 8'-long tow-tank was designed and fabricated. In this configuration, (Lagrangian) time following the passage of the turbulence-generating grid past the measuring station is equivalent to distance behind the turbulence-generating grid. The facility that has been described previously is depicted in Figure 7. Earlier versions of this facility were described previously. It is included here for completeness.

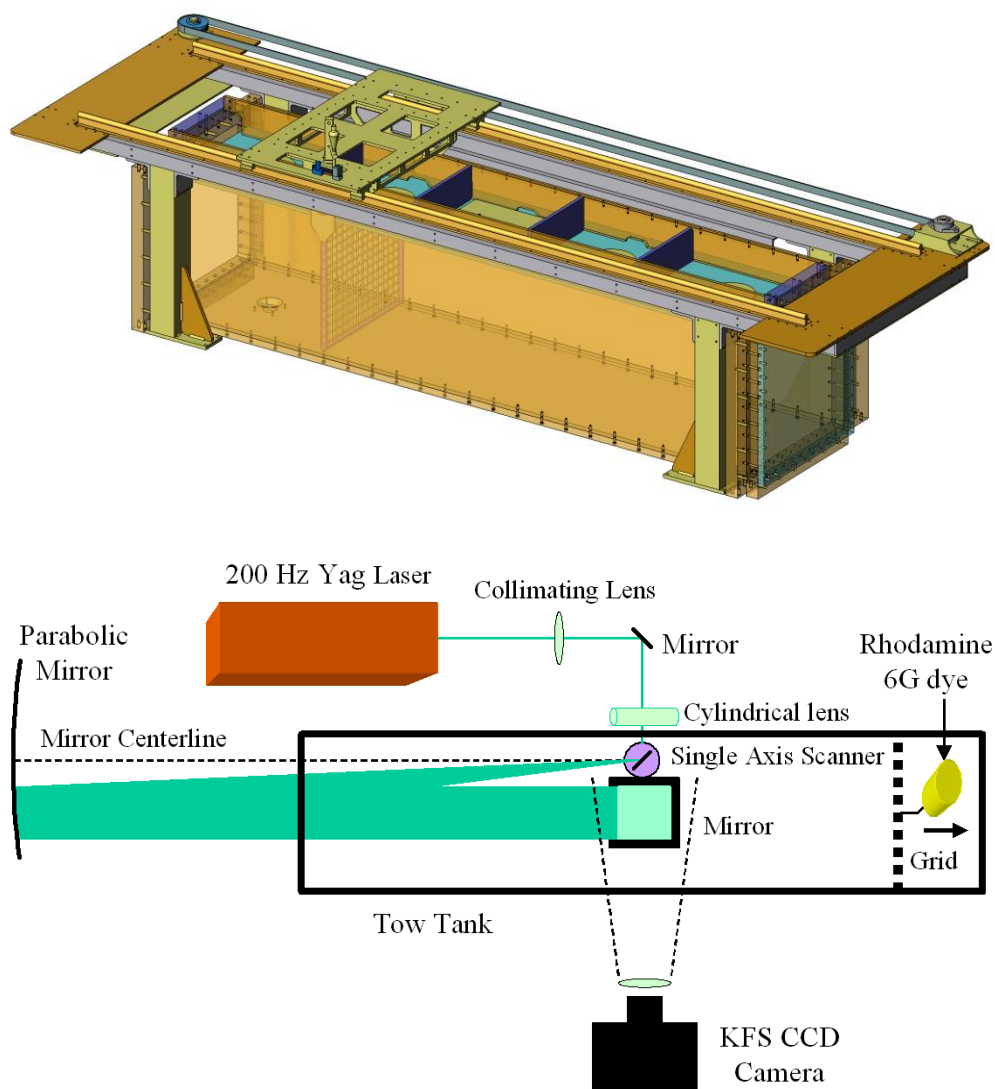


Figure 7. Tow-tank and optics for the scalar-dispersion experiments. Top: Tow-tank schematic depicting the digitally controlled carriage on low-friction rails, with the turbulence-generating grid and free-surface/wave suppression top. Bottom: Optics schematic depicting the 200Hz laser, 24" parabolic collimating mirror, and related optics, configured for side-view (streamwise) image recording.

The optical configuration allows slices (transects) to be recorded in the streamwise or flow-transverse directions by rotation of a single Littrow prism under the facility and moving the high-frame rate (KFS) CCD camera designed and fabricated in-house, along with its data-acquisition system. We note that each image is comprised of  $1024 \times 1024$  pixels, i.e., 1 Mpixel/frame. These are recorded at 200 Hz (frames/s), as limited by the quad laser cumulative pulse rate, corresponding, in turn, to  $2 \times 10^8$  measurements per second, at 12 bits per measurement. The data stream is compressed via loss-less compression, passed through 8 optical fiber channels, and recorded on a parallel computer-controlled (Datawulf) disk array capable of recording several terabytes at this rate.

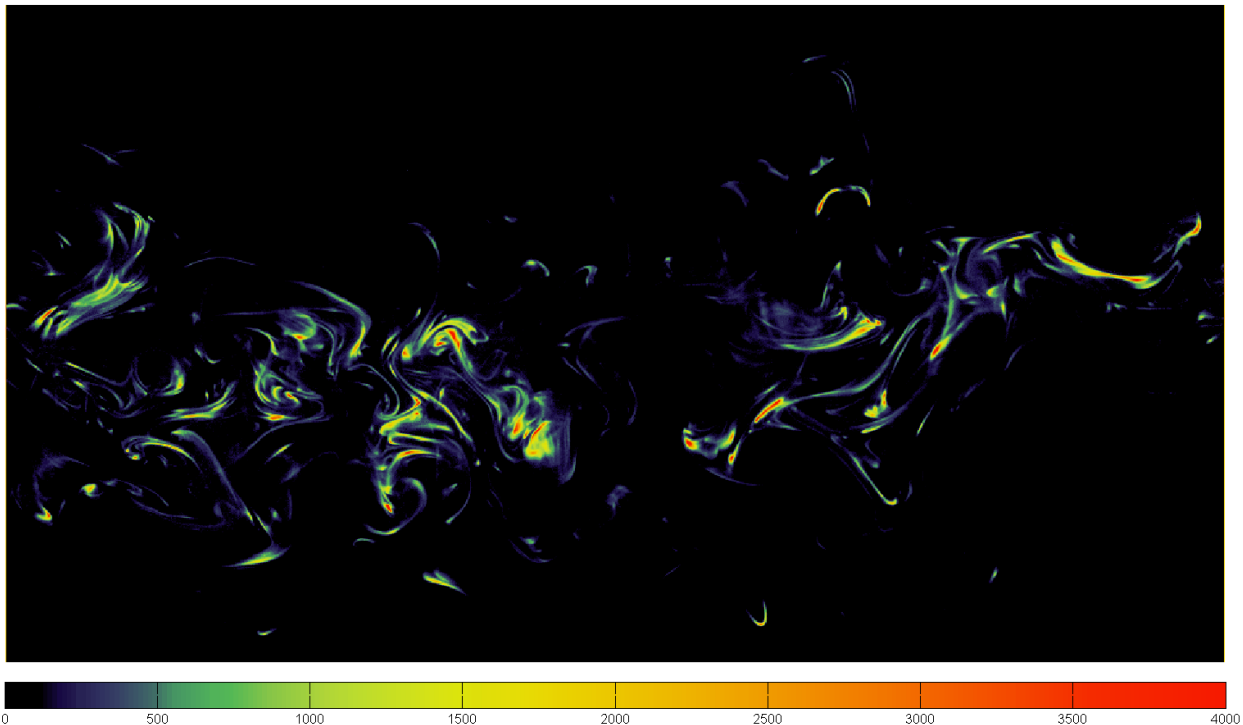


Figure 8. Streamwise slice of the scalar concentration field, rendered in false color, as indicated in the legend below. Scalar data image captures the field in the downstream range of  $20 < x/M < 40$  (grid mesh lengths). Data from Krawczynski, Lang, and Dimotakis (unpublished).

The large dynamic range (up to  $1:10^6$ ) afforded by the laser-induced fluorescence diagnostics and high signal-to-noise ratio digital imaging, despite the high framing rates, allowed data to be recorded over a range of mesh lengths extending to  $x/M \cong 150$ , or so, where  $M$  is the turbulence-grid mesh length, with reliable statistics possible for data to 100 mesh lengths, and a little beyond. This range exceeded the reach of previous experimental investigations and allowed reliable far-field plume-scaling statistics to be determined. It is perhaps also worth noting that the large dynamic range encountered in this flow also places the phenomenon beyond the reach of reliable computational investigation, at least today.

The large dynamic range necessitated an elaborate frame-by-frame calibration technique to be developed and validated. An example of a single streamwise slice of the scalar field is depicted in new data reproduced in Figure 8, illustrating the high quality of the measurements. Grid velocity for these data is  $U_G = 5.4$  cm/s, corresponding to a mesh Reynolds number of  $Re_M = \rho U_G M / \mu \cong 1700$  and a Taylor Reynolds number of  $Re_T \approx 41$ . Data from higher Reynolds number runs are discussed below. The measurements resolve all flow scales up to moderate Reynolds numbers, even though they may not resolve the initially sharp scalar gradients in this high Schmidt-number fluid medium (water:  $Sc \equiv \nu/D \cong 2000$ ).

Generally, such scalar plumes are reported to exhibit axisymmetric statistics of mean behavior, with an average scalar concentration field that obeys self-similar behavior, given by,

$$\bar{c}(r, x) = c_0(x) f[r/\sigma(x)], \quad (1a)$$

where  $\bar{c}(r, x)$  is the average concentration of the scalar as a function of the radial distance  $r$  from the plume centerline, the distance  $x$  from the grid,  $c_0(x)$  is the average concentration on the plume centerline ( $r = 0$ ), and  $f[r/\sigma(x)]$  is the dimensionless plume radial concentration profile with  $\sigma(x)$  the radial scaling length. Similarity and dimensional analysis considerations admit a power-law dependence of  $c_0(x)$ , with the distance  $x$  scaled by the grid mesh size,  $M$ ,<sup>4</sup> with a possible virtual origin,  $x_0$ , i.e.,

$$c_0(x) = \bar{c}_0 [(x - x_0)/M]^{-p}. \quad (1b)$$

Scalar-flux considerations then constrain with  $\sigma(x)$  to a relation given by,

$$\sigma(x) = \bar{\sigma}_0 [(x - x_0)/M]^{p/2}, \quad (1c)$$

since the scalar flux,  $F$ , must be conserved, i.e., be independent of  $x$ , and we must have,

$$F \cong c_0(x) \sigma^2(x) = \text{fn}(x). \quad (2)$$

Theoretical proposals suggest a plume growth that increases, roughly, as  $\sigma(x) \propto x^{1/2}$  (excluding virtual-origin effects), and, therefore, a mean concentration centerline average that should be given by  $c(x) \propto x^{-1}$ . However, no sound foundation exists for the proposal, other than random-walk, or equivalent, arguments. Previous experiments offer no reliable reconciled results.

A key difficulty important in fuel injection is the role, if any, that the injection rate,  $J$ , may play in the behavior of the ensuing mixing field. Three general choices were considered:

1. An injection rate that results in a momentum-flux deficit in the turbulent flow, corresponding to a *wake*.
2. An injection rate momentum flux matches that in the turbulent flow, sometime called *isokinetic injection*, producing a momentum-less plume.
3. An injection rate that results in a momentum excess, producing a plume best described as a *jet* in the turbulent flow.

---

<sup>4</sup> The mesh size is  $M = 1.25'' = 3.18$  cm in these experiments.

The original experiments were conducted using a calibrated gravity-fed scalar (fluorescent dye) supply system. However, potential sensitivity to this experimental parameter and some of the questions that arose led us to the development and integration of a precision digitally-control injector that can deliver dye both precisely and reproducibly, allowing us to return to and spot-check previous runs, or perform new experiments to investigate the influence of the injection rate on the far-field plume.

We had initially considered the possibility of qualitative different behavior between wake-like and jet-like injection, that may have been characterized by slower dispersion corresponding to a wake or co-flowing jet, e.g.,  $c(x) \propto x^{-2/3}$  and  $\sigma(x) \propto x^{1/3}$ , vs. momentumless injection with an anticipated behavior of  $c(x) \propto x^{-1}$  and  $\sigma(x) \propto x^{1/2}$ . However, as described below, the experimental results did not offer definitive support for either conjecture.

One of the goals of this investigation was to assess the validity of the self-similarity scaling laws in Eq. 1 and, if valid, possible dependencies of the scaling exponent  $p$  on flow Reynolds number and injection rate. The phenomena proved to be complex, beyond any description in texts or publications on the subject. The discussion below offers a summary of the main accomplishments.

The main results on the streamwise behavior of the scalar plume to date are that:

- A. Good scaling behavior was found experimentally that supports the similarity behavior summarized in Eqs. 1a, 1b, and 1c.
- B. The scaling exponent,  $p$ , is found to depend on the injection rate and, possibly, on the flow Reynolds number based on grid mesh size,  $Re_M = \rho U_G M / \mu$ .
- C. The scaling exponent  $p$  exhibits a monotonic decrease with increasing injection rate,  $J$ , and does not appear to discriminate between the three injection cases outlined above.

These conclusions apply to mesh Reynolds numbers of  $Re_M \cong 15,900$  and  $31,800$ , which are quite high.

Injectant plumes exhibit a large run-to-run variance, despite the precision with which the injection rate and all other experimental conditions could be reproduced. This is attributable to the stochastic nature of the turbulence dynamics, as also attested by the complex scalar-field structure depicted in Figure 8, which is never the same twice. Previous analyses, theories, and experimental investigations had not anticipated the dependence of the far-field behavior on injection rate. The data suggest that the scaling exponent  $p$  (negative slope) may be approaching unity at high injection rates. However, more experiments would be required to confirm this expectation.

This part of the research represents a collaboration between Jean-Francois Krawczynski,<sup>5</sup> Daniel Lang, and Paul Dimotakis. The work is continuing and the results are, as yet, unpublished.

---

<sup>5</sup> Presently, Assistant Professor, Université Pierre et Marie Curie, Paris, France.

Following discussions with Dr. Chiping Li, our AFOSR Program Manager, the scalar-dispersion experimental investigations are continuing under AFOSR sponsorship (Grant No. FA9550-12-1-0461). A new emphasis focuses on the small-scale behavior typically incorporated in subgrid-scale (SGS) models used in contemporary large-eddy simulations (LES).

## 1.2 Modeling and numerical simulations

### 1.2.1 Jet injection in supersonic flow

As part of this effort, LES-SGS of an inclined circular jet (helium at  $M_j = 1$ ) into a supersonic turbulent boundary layer (air at  $M_\infty = 3.6$ ) was also performed. In the present numerical investigation, the jet geometry and flow parameters match those in the experiments of Maddalena *et al.* (2006) with a single injector.

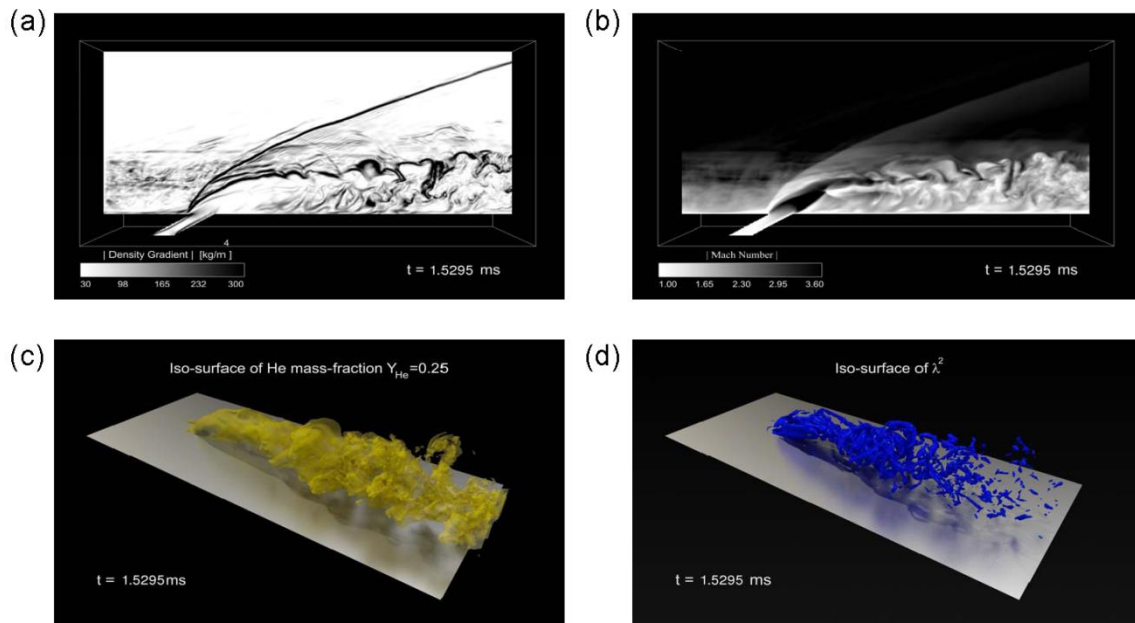


Figure 9. (a) instantaneous density-gradient magnitude in the mid-span plane; (b) instantaneous Mach number in the mid-span plane; (c) instantaneous isosurface of helium mass-fraction,  $Y_{\text{He}}=0.25$ ; (d) vortical structures identified by the  $\lambda_2$  method (Jeong & Hussain 1995).

The numerical study showed that the main flow features generated by the gas-dynamic interactions of an inclined jet with a supersonic cross-flow, such as barrel shock, Mach disk, shear layer, and counter-rotating vortex pair, are numerically captured by LES-SGS modeling framework. However, the transition and spatial development of the helium jet were shown to be strongly dependent on cross-flow inflow conditions. The results indicate that correct turbulent inflow conditions are required for reliable prediction of the dispersion and mixing of a gaseous jet in a supersonic, turbulent cross-flow. A novel methodology for the generation of synthetic turbulent inflow conditions for LES of spatially-developing, supersonic, turbulent wall-bounded

flows has been developed based on the approach of Ferrante & Elghobashi (2004). This was applied to the study of a supersonic turbulent flow over a flat wall interacting with an inclined jet, as illustrated in Figure 9. The images were generated by Paul Adams et al. at the Data Analysis and Assessment Center, U.S. Army Engineer Research and Development Center (HPCMP/DoD), MS 39180, USA.

This work was part of the postdoctoral research of A. Ferrante and was documented in Ferrante et al. (2010, 2011).

### 1.2.2 Dispersion, mixing, and chemical reactions behind a rearward-facing ramp

Large-Eddy simulations (LES), based on the stretched-vortex model (SVM) by Pullin and co-workers at Caltech, were performed to analyze the flow behind a rearward-facing ramp through which a specified mass flux is injected, as reported previously. The code was verified employing a variety of tests relying on exact linear-stability analysis results (Matheou et al. 2008). It was then applied to the simulation of chemically reacting flows at low heat release in this configuration.

Figure 10 depicts an instantaneous realization of the scalar mixture fraction in the turbulent flow downstream of the rearward-facing ramp through which the low-speed fluid is injected. That work was completed and published during the period of performance under this grant (Matheou et al. 2010).

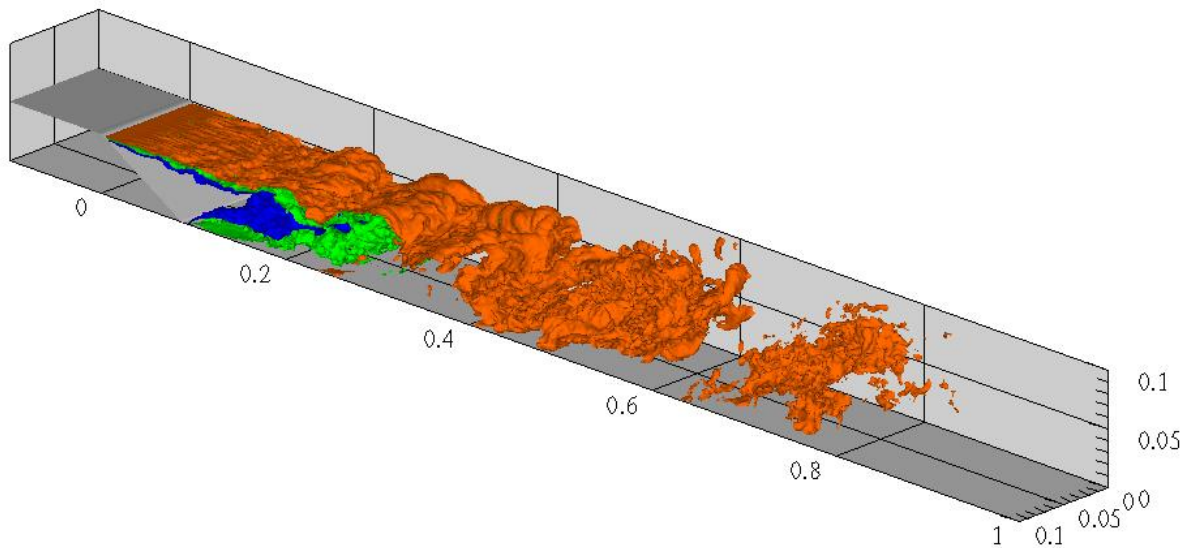


Figure 10. Instantaneous isosurfaces of mixture fraction,  $Z$ , in the LES of turbulent mixing in the expansion-ramp configuration with a subsonic top stream ( $M_1 = 0.3$ ). Three isosurfaces are color-coded and plotted at  $Z = 0.2$ ,  $0.5$  and  $0.8$ . The top stream carries a value of  $Z = 1$ . Figure from Matheou et al. (2010).

Significant accomplishments in this work include the correct capturing of the experimentally determined molecularly mixed and reacted fluid, and temperature rise, under subsonic ( $M \sim 0.3$ )

and high Reynolds number flow conditions, and grid convergence with a highest spatial grid resolution in the simulations that was two orders of magnitude above what would have been required for a direct numerical simulation (DNS) of this flow without modeling. To our knowledge, this represents the first time this has been achieved in a numerical simulation of small-scale phenomena, such as turbulent mixing with fast chemical reactions, in high Reynolds number flow.

### 1.2.3 Modeling of ignition delays in ethylene-fueled scramjets

A simplified model was developed for ethylene-fueled scramjets by way of example because the chemical kinetics of ethylene, while perhaps not perfectly known, are better known than those of the more practical but complicated jet fuels. The latter must be employed as endothermic fuels in hypersonic powered flight to address the complex thermal-management issues that arise. The study compares shear-layer and jet-in-crossflow fuel-injection schemes. The results illustrate the sensitivity of ignition delay to flight Mach number and fuel preheat for the two (jet-in-crossflow and shear-layer) fuel-injection schemes.

A simplified model was developed for normal-jet injection entrainment and ignition in supersonic crossflows with blowing ratios,

$$r = \sqrt{\frac{\rho_j u_j^2}{\rho_\infty u_\infty^2}}. \quad (3)$$

close to unity, by calibrating jet-entrainment parameters to experimental entrainment results. The model was applied to describe ensuing mixing and ignition.

The simplified mixing and ignition model was used in a parametric study of ignition delay,  $\tau_d$ , which is expected to be responsible for the preponderant fraction of the reaction-completion time,  $\tau_c$  (Figure 11) in supersonic ethylene-fueled combustors.

The parametric study relates the ignition delay and combustion-completion times to flight and inlet conditions, and injected-fuel conditions for a generic scramjet that is assumed to be ethylene-fueled by way of example. The range of fuel-air ratios (composition),

$$\phi = \frac{X_{\text{fuel}}/X_{\text{air}}}{[X_{\text{fuel}}/X_{\text{air}}]_{\text{st}}} \quad (4)$$

where the  $X_i$  are the corresponding mole fractions and the denominator represents that ratio at stoichiometric conditions, are dictated by the entrainment characteristics of the particular fuel-injection scheme.

Detailed finite-rate chemical kinetics are simulated using the Cantera software package (Goodwin 2009) and the GRI Mech. 3.0 kinetics model (Smith et al. 2000). The latter is used because it is widely known and by way of illustrating the methodology rather than an endorsement of its correctness and applicability to ethylene-air combustion.

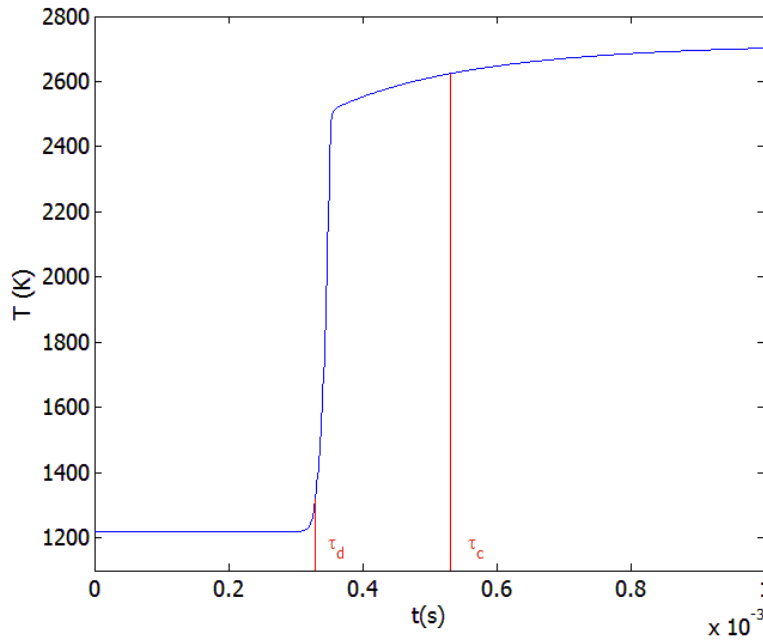


Figure 11. Illustration of ignition time delay,  $\tau_d$ , and combustion-completion time delay,  $\tau_c$ , for ethylene-air combustion. Simulations performed for a fuel-air ratio of  $\phi = 1.5$  (see Eq. 4) at a pressure of  $p = 2$  atm.

Inlet conditions are related to flight conditions based on ideal-gas relations. Fuel- and air-mixing mechanisms are based on the supersonic turbulent shear-layer combustion model by Dimotakis and Hall (1987) and an extension of the jet-in-crossflow mixing model by Shan and Dimotakis (2006). Ignition and combustion-completion time delays are important if the associated (Lagrangian) time is such that the distance a mixed fluid parcel travels before igniting and burning are too large. The rapid increase in the concentration of hydrogen radicals provided the ignition marker used for both fuel-injection schemes.

The fuel-injection schemes modeled are the jet-in-crossflow scheme (Figure 12), assumed to be normal injection into the crossflow, and the shear-layer mixing scheme (Figure 14). Both models are based on the balloon-reactor model (Dimotakis & Hall 1987). Jet-in-crossflow mixing is modeled as a parcel of injected fluid that entrains crossflow fluid and, as a consequence, grows in volume and mass while changing its trajectory downstream by momentum arguments such as those outlined by Hasselbrink and Mungal (1996), as in Figure 12. Jet-in-crossflow parameters in the present model were fit to experimental data by Lin et al. (2010).

For the jet-in-crossflow scheme, composition/stoichiometry changes as the fluid Lagrangian parcel moves along the jet trajectory (Figure 12), whereas the model for shear-layer injection described below (Figure 14) indicates that the composition/stoichiometry remains fixed until ignition. The flight Mach number is varied across a range  $5.5 < M_\infty < 7$  and injected-fuel stagnation temperature is varied across a range of  $900\text{K} < T_{0,f} < 1200\text{K}$ . The static

temperature ratio between flight conditions and combustor inlet is kept in the range of 6 to 7.5, while injected-fuel pressure is varied in a range of  $1.8 \text{ MPa} < p_i < 4 \text{ MPa}$  to maintain blowing ratios,  $r$  (Eq. 3), close to unity.

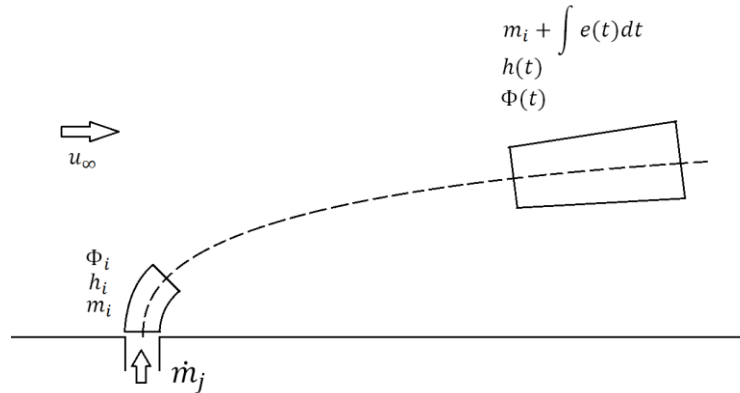


Figure 12. Jet-in-crossflow entrainment. Note the expected time-dependent stoichiometry and enthalpy of a jet-fluid containing Lagrangian fluid parcel.

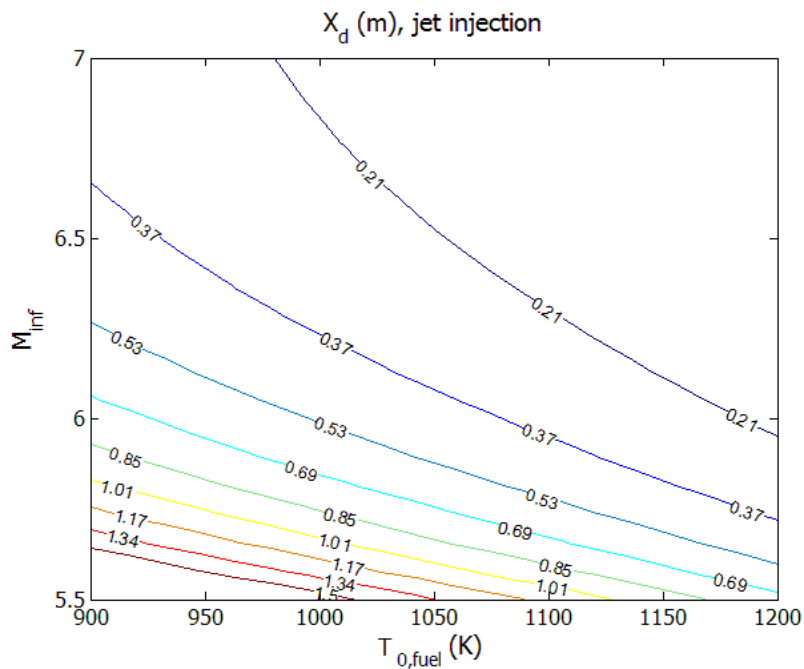


Figure 13. Distance a fluid parcel must travel downstream before igniting for a jet-in-crossflow fuel injection scheme.

Distances a fluid parcel will travel downstream before ignition are depicted in the contour plot in Figure 13. The contour lines indicate that for jet-in-crossflow injection, the distance a fluid parcel is predicted to travel before ignition is most sensitive to flight Mach number. This is because improved entrainment and mixing quickly decreases the equivalence ratio along the trajectory, rendering the effect of the crossflow static temperature at the combustor inlet more

important than the injected fuel preheat temperature. Nevertheless, fuel preheat provides an effective means to decrease ignition-delay times/distances at constant flight Mach number, but not nearly as effective as with shear layer injection.

The model applied to the shear-layer fuel injection scheme is the balloon-reactor model (Hall and Dimotakis 1987). In the present case, the intended model application extends to crossflow shearing over a reacting recirculation zone with spanwise near-uniform fuel addition, as schematically depicted in Figure 14.

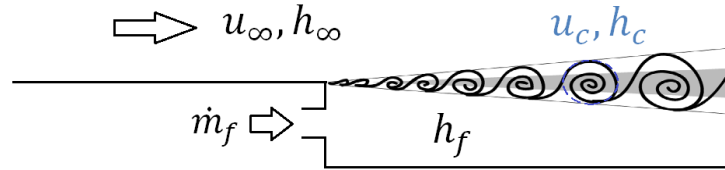


Figure 14. Shear-layer entrainment diagram in a convected large-structure convected frame for a reacting recirculating zone with span-wise uniform fuel injection.

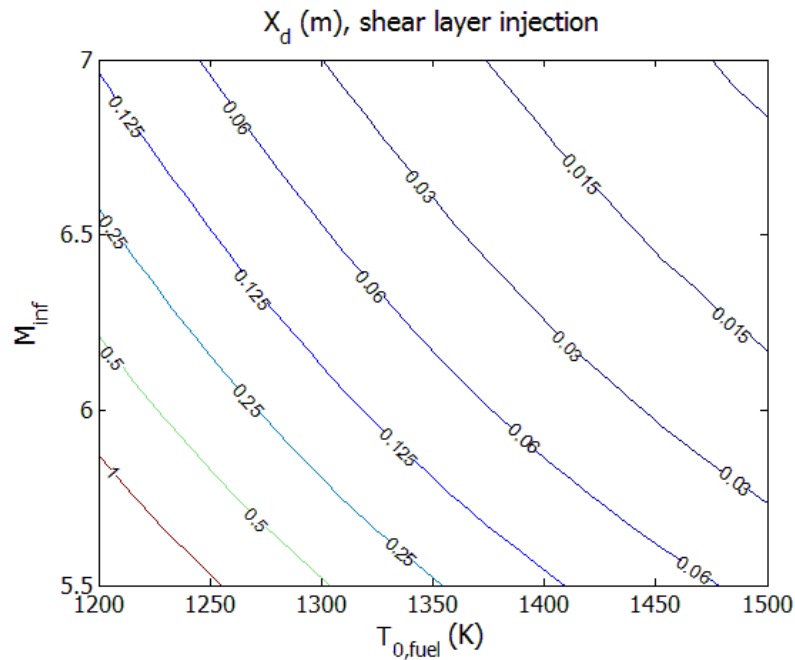


Figure 15. Distance a fluid parcel must travel downstream before igniting for a shear-layer fuel injection scheme.

For shear-layer fuel injection, flight Mach number varies across a range of  $5.5 < M_\infty < 7$  and the injected fuel stagnation temperature varies across a range of  $1200 \text{ K} < T_{0,f} < 1500 \text{ K}$ , where  $T_{0,f}$  is the initial fuel-injection temperature. Ignition delays are found to be equally sensitive to fuel preheat and flight Mach number, as shown in Figure 15. Fuel preheat for shear-layer fuel injection can be implemented in fuel-rich recirculation zones, as opposed to preheating

fuel prior to insertion into the combustion chamber, as would likely be the case with the jet-in-crossflow fuel injection.

These results suggest that the key to minimizing ignition delay without changing the flight Mach number in this environment is raising stagnation temperatures in the convected air-fuel mixture frame by pre-heating injected fuel and, most effectively, by designing the combustor with high-temperature shearing recirculation zones.

The preliminary parametric study conducted under this grant and described above assumed that the fuel has been preheated to the temperatures indicated, but has not been allowed to reach thermochemical equilibrium at that temperature. In work following the completion of the period of effort under this grant, the model was extended to allow thermochemical equilibrium to be reached before injection. The reactive radicals created in the process are found to significantly decrease ignition delays, as expected.

This important extension of the parametric model was documented after the end of the present period of performance by Cymbalist and Dimotakis (2013) and was cofunded by AFOSR Grant No. FA9550-12-1-0461 during the period of overlapping support. It is mentioned here as an update of the preliminary results included above. A detailed discussion of the analysis and significant differences in the results assuming thermochemical equilibrium were documented there.

### **1.3 Diagnostics developments**

The diagnostics developments were co-funded by AFOSR Grant No. FA9550-12-1-0461, during the period from 1 October 2012 to 15 June 2013 of overlapping support.

#### **1.3.1 Precision thermometry in supersonic flows**

The new thermocouple rake holds 66 thermocouples in 3 groups of three columns each (Figure 16). The thermocouples were calibrated against a set of temperature data from precision thermometers to obtain a mean RMS accuracy of under 0.15 K, as noted above.

The calibration was conducted in a specially designed assembly placed in a dewar with an externally controlled heater and three precision mercury thermometers. The temperature inside the dewar was raised to a value above the maximum temperature that needed to be calibrated. The heater was then turned off to stop all convection currents in the interior and the system was allowed to cool slowly, over several hours.

Thermometer readings were obtained during the cooling period and recorded along with bursts of thermocouple data through the same data-acquisition system used during the runs. In this fashion, the whole signal chain could be calibrated.

The calibration procedure is performed in 2 steps. The first step is to filter the calibrating data set for points whose mean absolute deviation (MAD) from the mean reading is indicative that the

measurements were taken when system was not yet in thermal equilibrium. Once the filtering is performed, the thermocouple data is fitted to the calibrating dataset by a third-order polynomial.

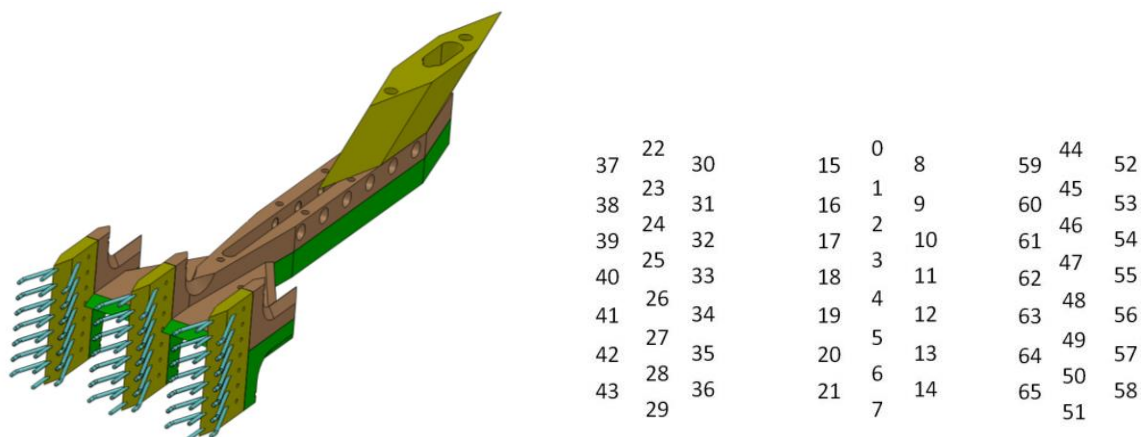


Figure 16. New thermocouple rake. Left: CAD drawing. Right: Thermocouple sensor layout.

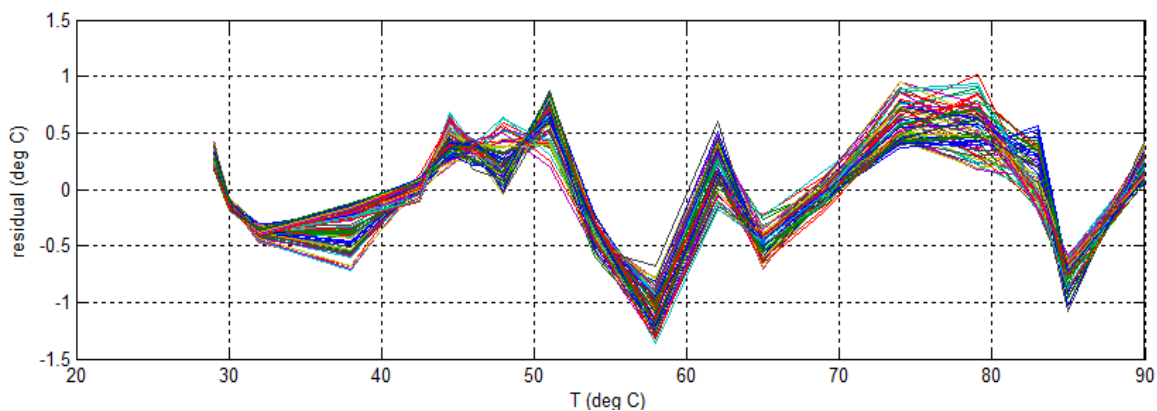


Figure 17. Temperature residuals for all 66 thermocouples, after Step 1 of the calibration.

At this point, the RMS magnitude of the residual is still above 1 K (Figure 17), but the MAD from the mean residual is below 0.15 K. This is the result of inaccuracies in reading the thermometers that were used (calibrating dataset). Since the individual read errors are common to all sensors at each temperature during the cooling period, this can be corrected by adjusting the reference temperature by the common (over all 66 thermocouples) mean residual and repeating the calibration using the new slightly adjusted reference temperatures (Figure 18). This is the second step in the calibration procedure.

The new polynomials result in a mean RMS deviation for the sensors that is less than 0.15 K, as documented below. Such accuracy is important if the two-dimensional temperature field is to be estimated by comparison of individual temperature measurements from different sensors with each other.

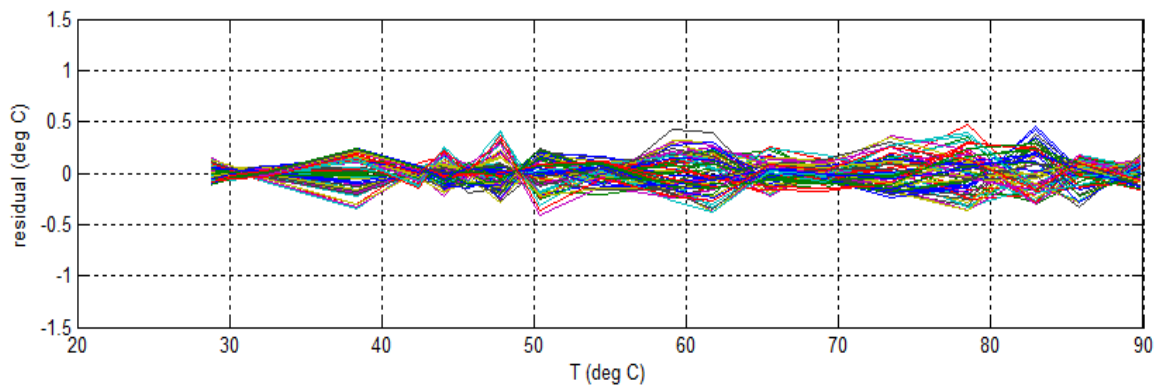


Figure 18. Temperature residuals after Step 2 of the calibration for all 66 thermocouples.

We believe that even better results are possible. However, residual RMS errors are sufficiently small to serve the purposes of the experimental effort, considering all other sources of uncertainty, and better than what is typically achievable with thermocouple sensors, especially considering that this applies across the whole set.

The part of the research was the work by Mehrotra, Cymbalist, Valiferdowski, Lang, and Dimotakis

### 1.3.2 Progress in optics and digital imaging

The schlieren system used as one of the concurrent diagnostics in the supersonic shear-layer (S3L) facility was upgraded to use a solid-state laser (LED) light source whose intensity and pulse duration can be digitally controlled and synchronized to the digital-imaging camera. This has increased luminosity in each captured frame in high framing-rate sequences that record the evolution of the flow and unsteady effects. An example is reproduced in Figure 19, from the same run as for the third image from the top in Figure 5 (Run 1656). The experimental parameters for this run are listed in the legend on the left in Figure 5.

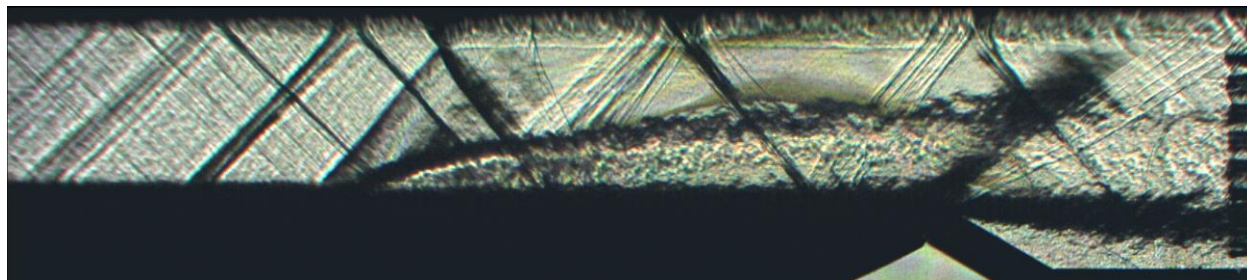


Figure 19. Schlieren image of supersonic ( $M_1 = 1.5$ ) chemically reacting flow with jet injection through five diamond jets, extracted from a high framing-rate sequence. Image extracted from the same experimental run as in the third image from the top in Figure 5 (Run 1656).

While the low-resolution reproduction in Figure 19 does not do justice to the original data, important flow features that not often discernible were recorded. As an illustrative example, the thin shear layer formed downstream of the intersection of the weak oblique waves just below the

turbulent boundary layer near the top guidewall, above and a little downstream of the diamond-jet leading edge in Figure 19, is quite clear. Also clear is the expansion-wave system formed at the corner of the expansion ramp that measures mixing and dilatation and (in the fully resolved image) the conical shocks generated by each of the thermocouple sensors, clearly indicating that the flow remains supersonic despite the mass injection and heat release. There was no mass injection through the downward-facing ramp in this experiment.

Digital-imaging framing rates for this diagnostic up to 10 kfps (10 thousand frames per second) have been used thus far. Higher framing rates yet can be achieved in our experiments but at a loss in spatial resolution. Since framing rates approaching 100 kfps would be needed to resolve the unsteady velocity field and some of the other dynamics in this flow, no higher framing rates have been used for data recording to date. We are exploring other possibilities, however, to support future experiments.

All diagnostics data are acquired simultaneously and synchronized. This allows multi aspects of the phenomena investigated to be assessed together. As an example, correlating temperature maps and schlieren images, a time-dependent visualization of the flow was obtained at 400 Hz, subsampling the much-higher sampling rate schlieren digital image sequences. This visualization offers qualitative insight on the time dependent features of the flow over a larger timescale in the spanwise, wall-normal and streamwise directions in addition to the quantitative data obtained from the temperature field. Figure 20 is a screenshot from the animation for a flow with no jet injection and slightly divergent upper/lower guidewalls used to provide a baseline case for flows to accommodate mass injection and blockage.

The frame on the left reproduces the streamwise quantitative flow visualization and illustrates further improvements in flow quality, optics, and digital imaging realized since the image reproduced in Figure 19 was recorded.

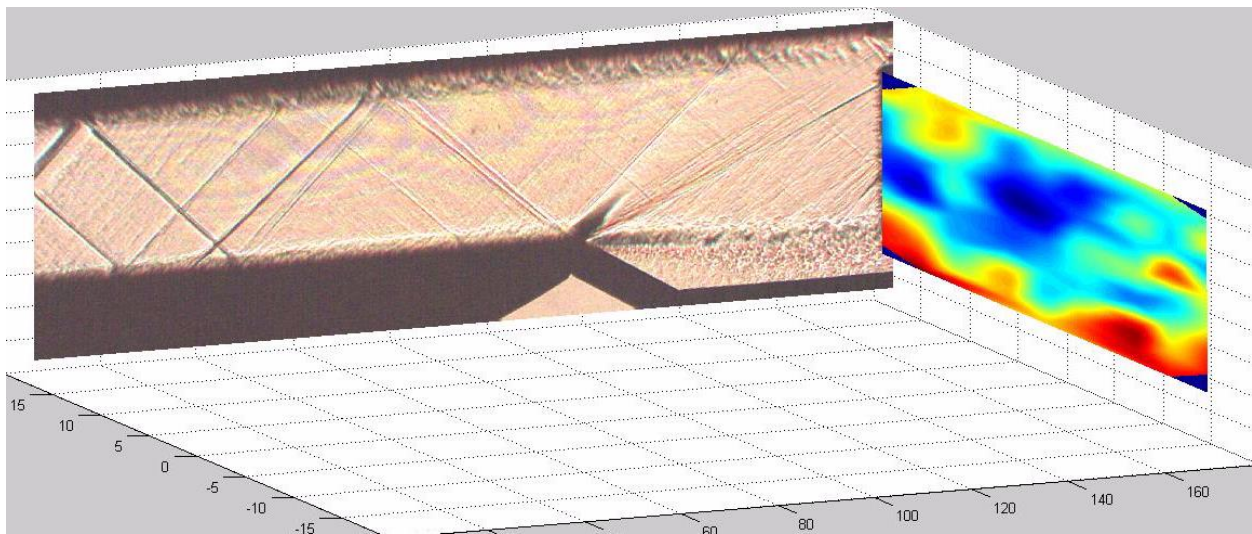


Figure 20. Screenshot of time-dependent, correlated schlieren and temperature map quantitative visualization (Cymbalist, Lang, and Dimotakis, unpublished data).

The frame on the right, color codes the simultaneous temperature field in the flow-transverse plane and records the (slightly) higher temperature in the recirculation zone downstream of the rearward-facing 30-degree ramp. The precision calibration described above makes the reliable sensor-by-sensor comparison possible and enables the whole transverse temperature field to be mapped, as illustrated in this figure, which also documents that no spurious sidewall flow contamination is occurring; something that could not be ascertained by the spanwise-averaging schlieren data. The range spanned in the sequence of transverse temperature fields from which the false-color-coded field sample was extracted is only 25 K ( $232\text{ K} < T < 257\text{ K}$ ).

This part of the research effort was conducted by Cymbalist, Lang, and Dimotakis and is, as yet, unpublished.

### **1.3.3 Digital control of the short running-time supersonic-flow facility**

A significant challenge in our experimental effort was met during this period. In particular, real-time control of the facility during the few-second duration experimental runs had been implemented under a legacy Digital Equipment Corporation LSI-11 computer that allowed every CPU cycle to be under program control. Even though modern computing equipment is much faster, the complexity of modern operating systems did not allow the same level of control until very recently.

During the last year of this effort, facility control during the short running-time runs was transferred to the same computer that controls data acquisition, also allowing a seamless integration of facility-control data sequences and the acquisition of data from multiple sensors and high framing-rate cameras. The stability of the facility improved in the process, allowing for shorter control-loop time cycles that removed higher-frequency fluctuations of controlled variables. This part of the work represents a multi-year effort performed by D. Lang.

## 2. Bibliography and publications of supported work

Publications of work supported by this grant, or which appeared during the period of support by this grant, are perpended by an asterisk.

\* Bergthorson, J., S. Salusbury, and P.E. Dimotakis 2011 Experiments and modelling of premixed laminar stagnation flame hydrodynamics. *J. Fluid Mech.* 681:340-369, doi:10.1017/jfm.2011.203.

\* Bonanos, A.M., J.M. Bergthorson, and P.E. Dimotakis 2009 Molecular mixing and flowfield measurements in a recirculating shear flow. Part II: supersonic flow. *Flow, Turb. & Combustion* 83:251–268, doi:10.1007/s10494-009-9199-x

\* Cymbalist, N., and P. Dimotakis 2013 A parametric study of ethylene-fueled scramjet combustion. 43rd *AIAA Fluid Dynamics Conference* (San Diego, CA), Paper AIAA-2013-2978.

Dimotakis P.E., and J.L. Hall 1987 A Simple Model for Finite Chemical Kinetics Analysis of Supersonic Turbulent Shear Layer Combustion. *AIAA/SAE/ASME/ASEE 23<sup>rd</sup> Joint Propulsion Conference* (29 June - 1 July 1987, La Jolla, CA), AIAA Paper 87-1879.

\* Dimotakis, P.E., and C. Pantano 2013 Turbulent Combustion. *Yearbook of Science & Technology* 2013 (McGraw-Hill, ISBN 978-0-07-180140-9), 373-376.

Ferrante, A., and S. Elghobashi 2004 A robust method for generating inflow conditions for direct simulations of spatially-developing turbulent boundary layers. *J. Comput. Phys.* 198:372–387.

\* Ferrante, A., G. Matheou, and P.E. Dimotakis 2010 LES of an Inclined Jet into a Supersonic Turbulent Crossflow: Synthetic Inflow Conditions. 48<sup>th</sup> *AIAA Aerospace Sciences Meeting*, Paper AIAA-2009-1511.

\* Ferrante, A., G. Matheou, and P.E. Dimotakis 2011 LES of an inclined sonic jet into a turbulent crossflow at Mach 3.6. *J. Turbulence* 12(2):1-32, doi: 10.1080/14685248.2010.522580.

\* Ferrante, A., C. Pantano, G. Matheou, and P.E. Dimotakis 2009 On the Effects of the Upstream Conditions on the Transition of an Inclined Jet into a Supersonic Cross-Flow. 47<sup>th</sup> *AIAA Aerospace Sciences Meeting*, Paper AIAA-2009-1511.

Goodwin, D., 2009 *Cantera, an object-oriented software toolkit for chemical kinetics, thermodynamics, and transport processes*. (Version 2.0) [Computer program]. Available at <http://code.google.com/p/cantera/> (accessed 20 November 2012).

Hasselbrink E.F., and M.G. Mungal 1996 An analysis of the time-averaged properties of the far field of the transverse jet. *AIAA 34<sup>th</sup> Aerospace Sciences Meeting and Exhibit* (Reno, NV), CP96-0201.

Heiser W.H., and D.T. Pratt 1994 *Hypersonic Airbreathing Propulsion*. AIAA (Washington, DC), pp. 149, 197.

Jeong, J., and F. Hussain 1995 On the identification of a vortex. *J. Fluid Mech.* 285:69–94.

Maddalena, L., T.L. Campioli, and J.A. Schetz 2006 Experimental and computational investigation of light-gas injectors in Mach 4.0 crossflow. *J. Propulsion & Power* 22:1027–1038.

Matheou, G., C. Pantano, and P.E. Dimotakis 2008 Verification of a fluid-dynamics solver using correlations with linear stability results. *J. Comp. Physics* 227:5385-5396, DOI: 10.1016/j.jcp.2008.01.055.

\* Matheou, G., A.M. Bonanos, C. Pantano, and P.E. Dimotakis 2010 Large-eddy simulation of mixing in a recirculating shear flow. *J. Fluid Mechanics* 646:375-414, doi: 10.1017/S0022112009992965.

Shan, J.W., and P.E. Dimotakis 2006 Reynolds-number effects and anisotropy in transverse-jet mixing.” *Journal of Fluid Mechanics* 566:47-96.

Smith G.P., D.M. Golden, M. Frenklach, N.W. Moriarty, B. Eiteneer, M. Goldenberg, C.T. Bowman, R.K. Hanson, S. Song, W.C. Gardiner, Jr., V.V. Lissianski, and Q. Zhiwei 2000 GRI-Mech 3.0. [http://www.me.berkeley.edu/gri\\_mech/](http://www.me.berkeley.edu/gri_mech/)

Ward-Smith A.J. 1979 Critical Flowmetering: The Characteristics of Cylindrical Nozzles with Sharp Upstream Edges. *Int. J. Heat and Fluid Flow* 1(3):123-132.

### 3. Research personnel

#### 3.1 Personnel supported by this grant

Bardet, Philippe: contributed as a Caltech post-doc. Presently, Assistant Professor, George Washington University.

Cymbalist, Niccolo: graduate student, Aeronautics, Caltech.

Dimotakis (PI), Paul: John K. Northrop Professor of Aeronautics and Professor of Applied Physics, Caltech.

Ferrante, Antonino: contributed as a Caltech post-doc. Presently, Assistant Professor, University of Washington.

Krawczynski, Jean-Francois: contributed as a Caltech post-doc. Presently, Assistant Professor, Université Pierre et Marie Curie, Paris, France, and continuing collaborator.

Lang, Daniel: Research Engineer, Caltech.

Matheou, George: Caltech Ph.D. 2008, then contributor as a Caltech post-doc. Presently, physicist at the Jet Propulsion Laboratory and continuing collaborator.

Mehrotra, Prakhar: Caltech graduate student and Aeronautical Engineer (graduated Caltech 2013).

Valiferdowski, Bahram: Research Engineer.

Support provided by this grant to all personnel listed above was part time.

### **3.2 Collaborations and related discussions**

Jeff Berghthorson, Assistant Professor, McGill University, Canada, and continuing collaborator.

Aris Bonanos, Assistant Professor, Energy Environment and Water Research Center, Cyprus Institute, and continuing collaborator.

Graham Candler, McKnight Presidential Professor, Distinguished McKnight University Professor, and Russell J. Penrose Professor, Aerospace and Mechanics, University of Minnesota.

Luca Maddalena, Assistant Professor, University of Texas at Arlington and continuing collaborator.

Daniel Meiron, Fletcher Jones Professor of Aeronautics and Applied and Computational Mathematics, Caltech.

Carlos Pantano, Assoc. Professor, Mechanical Science and Engineering, University of Illinois at Urbana-Champaign.

Dale Pullin, Theodore von Kármán Professor of Aeronautics, Caltech.